Coupled Thermal and Solutal Transport in Magnetic Nanofluids with Field-Dependent Viscosity in Porous Media: A Stability Perspective

Monika Arora[1,*,#] and Mahesh Kumar Sharma[2,#]

[1] Department of Mathematics, School of Chemical Engineering and Physical Sciences, Lovely Professional University, Phagwara, 144411, India

[2] Department of Mathematics, Maharaja Agrasen University, Baddi, 174103, India

INFORMATION

Keywords:
Double diffusive instability
field dependent viscosity
chebyshev pseudospectral–QZ algorithm
critical rayleigh number
magnetic nanofluids

DOI: 10.23967/j.rimni.2025.10.72702

SCIPEDIA Revista Internacional de Métodos Numéricos para Cálculo y Diseño en Ingeniería

Revista Internacional Métodos numéricos para cálculo y diseño en ingeniería RIMNI

In cooperation with CIMNE

Coupled Thermal and Solutal Transport in Magnetic Nanofluids with Field-Dependent Viscosity in Porous Media: A Stability Perspective

Monika Arora[1,*,#] **and Mahesh Kumar Sharma**[2,#]

[1]Department of Mathematics, School of Chemical Engineering and Physical Sciences, Lovely Professional University, Phagwara, 144411, India

[2]Department of Mathematics, Maharaja Agrasen University, Baddi, 174103, India
[#]These authors contributed equally to this work

ABSTRACT

This study investigates the linear stability of double-diffusive convection in magnetic nanofluids (MNFs) within a horizontal porous medium, accounting for field–dependent viscosity (FDV). A modified Buongiorno–type model incorporates Brownian motion, thermophoresis, magnetophoresis, and Darcy resistance. The resulting eigenvalue problem is solved via a Chebyshev pseudospectral–QZ algorithm under rigid–rigid (RR), rigid–free (RF), and free–free (FF) boundary conditions for both water–based (W_b) and ester–based (E_b) MNFs. Results show that magnetic and solutal effects lower the critical Rayleigh number (Ra_c) from the classical Darcy–Bénard limit of ≈39.48 to as low as ≈23.8, indicating enhanced instability. In contrast, increasing the FDV coefficient (δ), Langevin parameter (α_L), and nanoparticle concentration difference ($\Delta\phi$) raises Ra_c, stabilizing the system. E_b–MNFs exhibit consistently higher Ra_c values—by 15%–20% compared to W_b–MNFs, due to greater viscosity and lower thermal diffusivity. These findings clarify the interplay of magnetoviscous damping and solutal buoyancy, offering predictive insights for the design of magnetically tunable porous heat exchangers and thermal management systems.

OPEN ACCESS

Received: 02/09/2025

Accepted: 19/11/2025

Published: 16/04/2026

DOI
10.23967/j.rimni.2025.10.72702

Keywords:
Double diffusive instability
field dependent viscosity
chebyshev pseudospectral–QZ algorithm
critical rayleigh number
magnetic nanofluids

Nomenclature

Dimensional Quantities

Symbol	Description
c_f	Nanofluid specific heat
c_p	Nanoparticle specific heat
d	Thickness of the nanofluid layer
D_B	Brownian diffusion coefficient
D_H	Magnetophoretic diffusion coefficient
D_T	Thermophoretic diffusion coefficient
g	Acceleration due to gravity

*Correspondence: Monika Arora (monikaarora1879@gmail.com).

H	Magnetic field
$\mathbf{k}$	Unit vector in the z–direction
k_1	Thermal conductivity
k_B	Boltzmann's constant
K	Permeability of porous medium
$\mathbf{M}$	Magnetization
M_s	Magnetic saturation
p	Pressure
t	Time
T	Temperature
T_c	Temperature at the upper surface
T_h	Temperature at the lower surface
$\mathbf{q}$	Filtration velocity of the nanofluid

Non-Dimensional Parameters

Symbol	**Description**
D_a	Darcy number
Le	Lewis number
Les	Lewis number for solute
$M_1, M_1', M_1'', M_3, M_3', M_3''$	Magnetic parameters
N_A, N_A'	Modified diffusivity ratios
N_B	Modified particle density increment
N_{CT}	Soret parameter
N_{TC}	Dufour parameter
P_r	Prandtl number
Ra	Thermal Rayleigh number
Rn	Nanoparticle Concentration Rayleigh number
Rs	Rayleigh number for solute
V_a	Vadasz number
Greek symbol	**Description**
α	Coefficient of thermal expansion
α_L	Langevin parameter
β	Uniform temperature gradient
κ	Thermal diffusivity
μ	Viscosity of nanofluid
μ_0	Magnetic permeability of vacuum
ρ	Density
δ	field dependent viscosity coefficient
θ	Perturbation in temperature
ϕ	Nanoparticle volume fraction
ϕ_0	Reference nanoparticle volume fraction
χ	Tangent magnetization susceptibility
χ_2	Chord magnetization susceptibility
ϵ	Porosity

Subscript	**Description**
b	Basic state
f	Fluid
m	Porous medium
0	Reference quantity
Operator	**Description**
∇	$\frac{\partial}{\partial x}+\frac{\partial}{\partial y}+\frac{\partial}{\partial z}$
∇^2	$\frac{\partial^2}{\partial x^2}+\frac{\partial^2}{\partial y^2}+\frac{\partial^2}{\partial z^2}$
∇_1^2	$\frac{\partial^2}{\partial x^2}+\frac{\partial^2}{\partial y^2}$

1 Introduction

Transport in porous media subjected to simultaneous thermal and compositional gradients plays a pivotal role in geothermal systems, electrochemical processes, filtration technologies, and biomedical flows. When heat and solute diffuse at different rates, their respective buoyancy contributions may either compete or reinforce, resulting in *double-diffusive convection* (DDC) with complex stability characteristics [1,2]. Nield and Kuznetsov [3] performed an analytical investigation on DDC in nanofluids, revealing how Brownian motion, thermophoresis, and cross-diffusion modify classical thresholds. Sharma and Singh [4] extended this to porous media with magnetic nanofluids (MNFs), showing sensitivity to nanoparticle type and magnetic effects. Mahajan and Sharma [5] demonstrated that Dufour and Soret parameters strongly influence onset conditions, especially under microgravity, while Sunil et al. [6] highlighted subcritical instabilities via nonlinear energy methods for rotating ferrofluid layers. These studies underscore the importance of buoyancy–magnetic coupling and cross-diffusion in shaping DDC onset in MNF-saturated porous domains.

Magnetic nanofluids (MNFs)–suspensions of magnetic nanoparticles in conventional base fluids—introduce a tunable mechanism via external magnetic fields, enabling control over body forces and material properties [7,8]. This controllability has spurred interest in MNFs for applications in directed cooling, magnetically enhanced heat exchangers, and smart fluid systems. Two magnetically induced phenomena are particularly significant in MNFs. First, magnetic body forces, governed by field strength and orientation, enter the momentum balance and may suppress or enhance buoyant flow [9]. Second, many MNFs exhibit *field–dependent viscosity* (FDV), wherein the effective viscosity increases with field intensity due to particle chaining or aggregation. FDV introduces additional viscous damping, directly influencing the onset of convection. Empirical studies and theoretical models have consistently demonstrated that FDV alters critical thresholds and flow regimes [10–14]. Recent analyses further quantify the effect of FDV on near-wall transport and thermal performance in boundary layers [15], while magnetohydrodynamic (MHD) studies on hybrid nanofluids confirm strong sensitivity to magnetic parameters and nanoparticle properties [16]. Because the onset conditions determine the operational envelope for these devices, an accurate stability criterion that accounts for FDV is indispensable for reliable engineering design and control of magnetically-driven transport.

Porous structures amplify these complexities. Parameters such as porosity, permeability, and Darcy/Brinkman drag influence how thermal and solutal gradients interact with magnetic effects, often stabilizing longer wavelengths while generating non-trivial parameter couplings [3,5,17]. Studies

involving hybrid nanofluids in magnetized porous domains show that fluid composition, particle morphology, and magnetic alignment govern separation points and instability boundaries [18]. Syam [19] numerically investigated the heat and mass transfer characteristics of nanofluid flow over a rotating disk embedded in a Darcy–Forchheimer porous medium, highlighting the pronounced effects of magnetic field strength, velocity slip, and thermophoretic forces on velocity suppression and thermal enhancement in microfluidic and energy systems. Similar conclusions emerge from investigations of radiative MHD nanofluids in porous environments, where thermophoresis, Brownian motion, and thermal sources/sinks play crucial roles [20]. These studies underscore the need for formulations that consistently capture FDV, nanoparticle migration, magnetization, and porous drag in a unified framework.

Foundational theories—such as ferrohydrodynamic convection [8,9] and the Buongiorno model for nanoparticle transport—laid the groundwork for understanding MNF behavior [21]. Extensions to porous domains, including Nield–Kuznetsov-type models, have since identified the thermal and solutal Rayleigh numbers, Lewis numbers, and cross-diffusion effects as key stability parameters [3,22]. More recent studies incorporating Dufour/Soret coupling, rotation, and hybrid compositions illustrate how added physics influence thresholds and modal selection [6,23,24]. Crucially, the omission of FDV in many prior analyses has been identified as a major source of predictive inaccuracy; its explicit inclusion is essential for reliable modeling of convective onset in MNFs [11,12].

Complementing classical analyses, current research trends increasingly employ data-driven methods and thermal optimization to capture complex multiparameter interactions. Recent high-impact contributions demonstrate how hybrid nanofluids and confined geometries respond sensitively to thermomagnetic effects [25], and how surrogate models based on machine learning can optimize thermal performance [26]. Advanced models, such as those employing the Caputo–Fabrizio fractional model [27], the Casson fluid model with activation energy [28], and the modified operational matrix method (OMM) [29], provide computational efficiency and insight into complex fluid properties. Despite these advancements in modeling methodology, a fundamental gap persists: the exclusion of FDV from many porous-MNF stability models continues to limit accuracy in predicting convective thresholds and scales. This work addresses this critical limitation by developing the first unified, Darcy-scale linear stability model that rigorously couples double-diffusive effects with Field-Dependent Viscosity in a porous magnetic nanofluid.

Motivated by this, the present study develops a Darcy-scale linear stability model for MNFs in a horizontal porous layer under simultaneous thermal and solutal gradients. The formulation incorporates FDV explicitly within a Buongiorno-type nanofluid framework, includes magnetic body forces in the momentum balance, and accounts for porous drag using Darcy–Brinkman resistance. A Chebyshev pseudospectral–QZ algorithm ensures spectral convergence for smooth eigenfunctions. The analysis isolates the influence of the FDV coefficient, Langevin parameter, particle loading, Rayleigh and Lewis numbers, and Darcy effects on the critical Rayleigh number and preferred wavenumber. We further confirm asymptotic consistency with classical limits and benchmark trends, situating our results within the broader context of porous magnetohydrodynamic and nanofluid literature [15,18,20,27,28,30,31].

2 Physical System Description

We consider a horizontal porous slab of thickness d, saturated with an incompressible MNF formed by dispersing spherical nickel (Ni) nanoparticles of size $\sim$10 nm in water and ester carriers. The layer is heated from below and subjected to a solutal gradient across its height. The vertical

domain is taken as $z \in [0, d]$, while the horizontal directions are assumed infinite, allowing convection to be modeled by two-dimensional perturbations. The flow is governed by the Darcy–Boussinesq approximation, which is valid for slow motion in porous structures where inertial forces are negligible. Under this approximation, variations in density influence the dynamics solely through the buoyancy contribution to the momentum balance.

The viscosity of the suspension is assumed to vary linearly with the applied magnetic field and is modeled as $\mu_1 = \mu(1 + \boldsymbol{\delta} \cdot \boldsymbol{B})$, where μ is the reference viscosity in the absence of a magnetic field, $\boldsymbol{B}$ denotes the magnetic induction, and $\boldsymbol{\delta} = \delta_1 \boldsymbol{i} + \delta_2 \boldsymbol{j} + \delta_3 \boldsymbol{k}$ characterizes field dependent viscosity coefficient. The formulation reflects how the viscosity of magnetic nanofluids increases with magnetic field strength due to the partial alignment of nanoparticles. This magnetoviscous effect adds resistance to flow, influencing the critical conditions for the onset of convection.

The linear FDV formulation used here follows earlier modeling efforts [13] and aligns with experimentally observed trends under moderate fields [10]. For stronger fields, higher-order nonlinearities can be introduced as a future extension.

For isotropic media, the coupling is uniform so that $\delta_1 = \delta_2 = \delta_3 = \delta$. Gravity $\boldsymbol{g}$ acts downward along the z–axis, while a uniform external magnetic field $\boldsymbol{H}$ is applied vertically across the porous layer. Both bounding surfaces are maintained at constant temperature and solute concentration, imposing isothermal and isoconcentrative boundary conditions (see Fig. 1). The porous structure itself is assumed homogeneous and isotropic, with uniform permeability and constant thermophysical parameters.

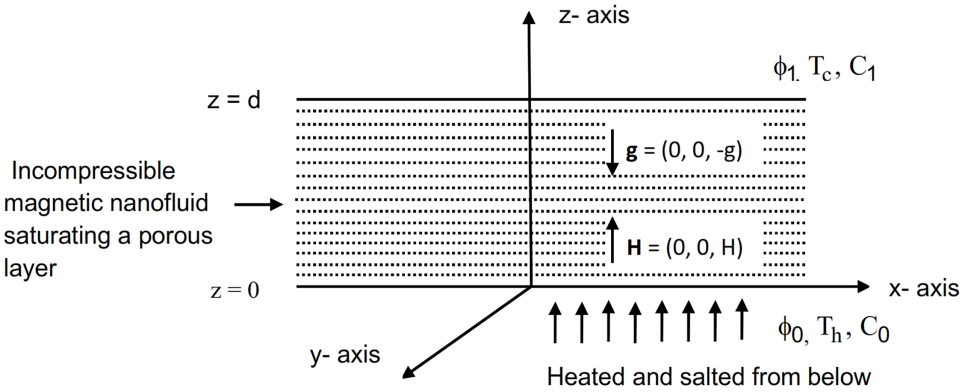

Figure 1: Schematic of the physical system: a horizontal porous layer saturated with an incompressible MNF, heated from below and subjected to a solutal gradient. The system is subject to gravity $\boldsymbol{g} = (0, 0, -g)$ and a uniform transverse magnetic field $\boldsymbol{H} = (0, 0, H)$. The lower boundary is maintained at temperature T_h and concentration C_0, while the upper boundary is fixed at T_c and C_1

3 Analytical Framework and Mathematical Setup

We consider MNF as a two-component mixture consisting of magnetic nanoparticles dispersed in a base fluid and adopt the following standard assumptions:

(i) the MNF is incompressible,

(ii) the suspension is dilute (i.e., the nanoparticle volume fraction satisfies $\phi \ll 1$),

(iii) no chemical reactions occur,

(iv) radiative heat transfer is negligible,
(v) viscous dissipation is negligible, and
(vi) the two constituents remain in local thermal equilibrium.

The system dynamics are governed by transport equations for continuity, momentum, nanoparticle concentration, energy, solute, and electromagnetic fields. These equations and the associated boundary conditions follow well-established formulations from previous studies [3,4,21,32,33], which incorporate the effects of porous resistance, nanoparticle migration, and electromagnetic body forces in magnetized nanofluids.

Continuity.

$$\nabla \cdot \boldsymbol{u} = 0, \tag{1}$$

where $\boldsymbol{u} = (u, v, w)$ is the Darcy velocity.

Momentum balance.

$$\frac{\rho_f}{\epsilon}\frac{\partial \boldsymbol{u}}{\partial t} = -\nabla p - \frac{\mu_1}{K}\boldsymbol{u} + \mu_0(\boldsymbol{M}\cdot\nabla)\boldsymbol{H} - \rho g \boldsymbol{k}, \tag{2}$$

with ϵ porosity, K permeability, and $\mu_1 = \mu(1 + \boldsymbol{\delta}\cdot\boldsymbol{B})$ the variable viscosity.

Nanoparticle concentration.

$$\frac{\partial \phi}{\partial t} + \frac{1}{\epsilon}\boldsymbol{u}\cdot\nabla\phi = \nabla\cdot\left(D_B\nabla\phi + D_T\frac{\nabla T}{T_c} - D_H\nabla H\right), \tag{3}$$

where D_B, D_T, and D_H denote Brownian, thermophoretic, and magnetophoretic diffusivities.

Energy equation.

$$(\rho c)_m\frac{\partial T}{\partial t} + (\rho c)_f(\boldsymbol{u}\cdot\nabla T) = \nabla\cdot(k_1\nabla T) + \epsilon\rho_p c_p\left(D_B\nabla T\cdot\nabla\phi + D_T\frac{\nabla T\cdot\nabla T}{T_c} - D_H\nabla T\cdot\nabla H\right) + (\rho c)_f D_{TC}\nabla^2 C, \tag{4}$$

where D_{TC} is the Dufour type diffusivity. Here, the terms proportional to D_B and D_T represent the effects of Brownian diffusion and thermophoresis, respectively, on the energy balance, following the formulation of Buongiorno [21]. The term proportional to D_H accounts for magnetophoretic transport, introduced here as an additional contribution. These terms arise from the scalar product $-c_p\,\mathbf{j}_p\cdot\nabla T$, where the nanoparticle flux is given by $\mathbf{j}_p = -\rho_p[D_B\nabla\phi + D_T(\nabla T/T_m) - D_H\nabla h]$ with $h = H/H_0$. In addition, the term involving D_{TC} corresponds to the Dufour effect, i.e., the contribution of concentration gradients to heat transfer [3]. Each of these contributions has the dimensions of a volumetric heat source ($\mathrm{W\cdot m^{-3}}$), ensuring the overall dimensional consistency of the energy equation.

Electromagnetic field.

$$\nabla\cdot\boldsymbol{B} = 0, \quad \nabla\times\boldsymbol{H} = 0, \quad \boldsymbol{B} = \mu_0(\boldsymbol{M} + \boldsymbol{H}). \tag{5}$$

Magnetization.

$$\boldsymbol{M}_{eq} = \frac{\boldsymbol{H}}{H}\left[M_0 + \chi(H - H_0) - K_m(T - T_h) + K_p(\phi - \phi_0) + K_c(C - C_0)\right], \tag{6}$$

with $K_c = \chi H_0/C_0$ coupling solute concentration to the magnetic field. The magnetization relation is a linearized extension based on Curie-type response around a base field, consistent with classical treatments of ferrohydrodynamics [9,13].

Solute concentration.

$$\frac{\partial C}{\partial t} + \frac{1}{\epsilon}\boldsymbol{u}\cdot\nabla C = D_{SM}\nabla^2 C + D_{CT}\nabla^2 T, \tag{7}$$

where D_{SM} is solutal diffusivity and D_{CT} the Soret-type diffusivity.

Boundary conditions.

$$\begin{aligned} &w = 0,\ T = T_h,\ \phi = \phi_0,\ C = C_0 \quad \text{at } z = 0,\\ &w = 0,\ T = T_c,\ \phi = \phi_1,\ C = C_1 \quad \text{at } z = d, \end{aligned} \tag{8}$$

together with the following velocity constraints:

$$\left.\frac{\partial w}{\partial z}\right|_{z=0} = 0, \qquad \left.\frac{\partial^2 w}{\partial z^2}\right|_{z=d} = 0. \tag{9}$$

Modeling Assumptions and Dimensional Consistency

The assumption of local thermal equilibrium (LTE) between nanoparticles and the base fluid is valid for particle diameters below 100 nm, since the interphase heat exchange time scale is orders of magnitude smaller than the macro-scale conduction time. This is consistent with foundational models of nanofluid transport in bulk fluids [21] and classical convection in porous media [34].

All governing equations were verified for dimensional consistency. The momentum equation yields units of acceleration $[L/T^2]$, while the energy and solute transport equations reduce to [K/s] and [kg m^{-3}s^{-1}], respectively. The Darcy number, $Da = K/d^2$, is based on realistic permeability values $K \sim 10^{-10}$–10^{-8} m^2 and domain height $d \sim 10^{-2}$ m, consistent with natural porous materials such as foams, sandstone, and fibrous matrices.

These validations confirm that the adopted simplifications are physically grounded and appropriate for the considered range of porous magnetic nanofluid configurations.

Non-dimensionalization.

Eqs. (1)–(7) are rendered dimensionless to obtain Eqs. (10)–(16) by scaling all lengths with d, time with d^2/κ, pressure with $d^2/(\mu\kappa)$, velocity with κ/d, temperature with $(T_h - T_c)$, concentration with $(\phi_0 - \phi_1)$, the magnetic field with H_0, and magnetization with M_0. The corresponding starred variables are

$$(x^*, y^*, z^*) = \frac{(x, y, z)}{d}, \qquad (u^*, v^*, w^*) = \frac{(u, v, w)\, d}{\kappa}, \qquad t^* = \frac{\kappa}{d^2}\, t,$$

$$T^* = \frac{T - T_h}{T_h - T_c}, \qquad p^* = \frac{d^2}{\mu\,\kappa}\, p, \qquad \phi^* = \frac{\phi - \phi_0}{\phi_0}, \qquad C^* = \frac{C - C_0}{C_0 - C_1},$$

$$H^* = \frac{H}{H_0}, \qquad M^* = \frac{M}{M_0},$$

where $\kappa = k_f/(\rho c)_f$ denotes the thermal diffusivity of the base fluid. Substituting these scalings into the dimensional balance laws and, for brevity, omitting asterisks thereafter yields the non-dimensional systems (10)–(16).

Rationale for non-dimensionalization.

To facilitate systematic analysis and to elucidate the relative significance of the underlying physical mechanisms, the governing equations are recast in terms of dimensionless variables. This transformation preserves the fundamental physics of mass, momentum, energy, nanoparticle, and solute transport, while condensing the formulation into a framework governed by key nondimensional groups. In particular, the scaled system highlights the influence of the thermal and solutal Rayleigh numbers, Lewis numbers, magnetization parameters, and field dependent viscosity coefficient, thereby providing a transparent foundation for the stability analysis and subsequent parametric exploration.

$$\nabla \cdot \boldsymbol{u} = 0, \tag{10}$$

$$\frac{1}{V_a}\frac{\partial \boldsymbol{u}}{\partial t} = -\nabla p - \boldsymbol{u} + \lambda_1(\boldsymbol{M}\cdot\nabla)\boldsymbol{H} - \{\nu_1(\boldsymbol{\delta}\cdot\boldsymbol{M}) + \nu_2(\boldsymbol{\delta}\cdot\boldsymbol{H})\}\boldsymbol{u} + \left(-R_n\phi + Ra\,T - Ra_N N_\phi\, T\phi - \frac{R_s}{Le_s} + R_s N_\phi \phi C + \rho_1\phi - \rho_2\right)\boldsymbol{k}, \tag{11}$$

$$\frac{\partial \phi}{\partial t} + \frac{1}{\epsilon}\boldsymbol{u}\cdot\nabla\phi = \frac{1}{Le}\nabla^2\phi + \frac{N_A}{Le}\nabla^2 T - \frac{N_A'}{Le}\nabla^2 H, \tag{12}$$

$$A\frac{\partial T}{\partial t} + \boldsymbol{u}\cdot\nabla T = \nabla^2 T + \frac{N_B}{Le}(\nabla T\cdot\nabla\phi) + \frac{N_A N_B}{Le}(\nabla T\cdot\nabla T) - \frac{N_A' N_B}{Le}(\nabla T\cdot\nabla H) + (\nabla T\cdot\nabla H) + N_{TC}\nabla^2 C, \tag{13}$$

$$\chi_2\,\nabla\cdot\boldsymbol{M} + \nabla\cdot\boldsymbol{H} = 0, \tag{14}$$

$$\boldsymbol{M} = \frac{\boldsymbol{H}}{H}\frac{(1+\chi)}{\chi_2}\left\{\frac{\chi}{1+\chi}H - \frac{M_1}{M_3}T + \frac{M_1'}{M_3'}\phi + \frac{M_1''}{M_3''}C + \frac{\chi_2 - 2\chi}{1+\chi}\right\}, \tag{15}$$

$$\frac{\partial C}{\partial t} + \frac{Pr}{DaV_a}\boldsymbol{u}\cdot\nabla C = \frac{1}{Le_S}\nabla^2 C + N_{CT}\nabla^2 T. \tag{16}$$

The auxiliary dimensionless parameters introduced in the formulation are defined as follows:

$$\lambda_1 = \frac{\mu_0 M_0 H_0 K}{\kappa\mu}, \qquad \rho_1 = \frac{dK\rho_f(\phi_0-\phi_1)(\alpha T_c - \alpha' C_1)g}{\kappa\mu}, \qquad A = \frac{(\rho c)_m}{(\rho c)_f},$$

$$\rho_2 = \frac{dK\rho_f}{\kappa\mu}(1 + \alpha T_c - \alpha' C_1)\,g \quad \text{and} \quad N_\phi = \frac{\phi_0 - \phi_1}{1-\phi_0}, \quad \nu_1 = \mu_0 M_0, \quad \nu_2 = \mu_0 H_0.$$

The corresponding non-dimensional boundary conditions are specified as follows:

$$\left.\begin{aligned} w = 0, \quad T = \frac{T_h}{T_h - T_c}, \quad \phi = \frac{\phi_0}{\phi_0 - \phi_1}, \quad C = \frac{C_0}{C_0 - C_1} \quad \text{at} \quad z = 0, \\ w = 0, \quad T = \frac{T_c}{T_h - T_c}, \quad \phi = \frac{\phi_1}{\phi_0 - \phi_1}, \quad C = \frac{C_1}{C_0 - C_1} \quad \text{at} \quad z = 1. \end{aligned}\right\} \tag{17}$$

Non-dimensional parameters.

The system dynamics are characterized by a set of non–dimensional parameters that encapsulate the influences of thermal, solutal, magnetic, and transport processes.

$$Ra = \frac{\rho_f g \alpha d K (T_h - T_c)}{\mu \kappa}, \qquad Pr = \frac{\mu}{\rho_f \kappa}, \qquad Da = \frac{K}{d^2}, \qquad V_a = \frac{\epsilon Pr}{Da}, \qquad Le = \frac{\kappa}{D_B},$$

$$M_1 = \frac{\mu_0 \chi^2 H_0^2 (T_h - T_c)}{\rho_f g \alpha d (1+\chi) T_c}, \qquad M_1' = \frac{\mu_0 \chi^2 H_0^2 (\phi_0 - \phi_1)}{\rho_f g \alpha d (1+\chi) \phi_0^2}, \qquad M_3 = \frac{\mu_0 \chi H_0^2}{\rho_f g \alpha d T_h},$$

$$M_3' = \frac{\mu_0 \chi H_0^2}{\rho_f g \alpha d \phi_0}, \qquad N_B = \frac{\epsilon (\rho c)_f (\phi_0 - \phi_1)}{(\rho c)_f}, \qquad R_n = \frac{(\rho_p - \rho_f)(\phi_0 - \phi_1) g d K}{\mu \kappa},$$

$$N_A = \frac{D_T (T_h - T_c)}{D_B T_c (\phi_0 - \phi_1)}, \qquad N_A' = \frac{D_H H_0}{D_B (\phi_0 - \phi_1)}, \qquad Ra_N = (1 - \phi_0) Ra,$$

$$R_s = \frac{\rho_f g \alpha' d K (C_0 - C_1)}{\mu D_{SM}}, \qquad Le_S = \frac{\kappa}{D_{SM}}, \qquad R_{sN} = (1 - \phi_0) \frac{R_s}{Le_S}, \qquad N_{TC} = \frac{D_{TC} (C_0 - C_1)}{k (T_h - T_c)},$$

$$M_1'' = \frac{\mu_0 \chi^2 H_0^2 (C_0 - C_1)}{\rho_f g \alpha' d (1+\chi) C_0^2}, \qquad M_3'' = \frac{\mu_0 \chi H_0^2}{\rho_f g \alpha' d C_0}, \qquad N_{CT} = \frac{D_{CT} (T_h - T_c)}{k (C_0 - C_1)}.$$

To streamline the formulation and eliminate redundancy, the dimensionless groups are organized based on their physical hierarchy. The thermal Rayleigh number (Ra) and the solutal Rayleigh number (Rs) are retained as independent primary control parameters, representing buoyancy forces arising from temperature and solute concentration gradients, respectively. The nanoparticle Rayleigh number (Rn) quantifies additional buoyancy effects due to nanoparticle concentration variations driven by thermophoretic and Brownian diffusion mechanisms.

The Lewis numbers, $Le = \alpha / D_B$ and $Les = \alpha / D_s$, characterize distinct diffusivity ratios for nanoparticle and solute transport, respectively, and are treated independently to preserve the integrity of the coupled heat and mass transfer physics.

The remaining parameters—Darcy number (Da), Vadasz number (Va), and magnetic coupling coefficients (M_1, M_1', M_1'', M_3, M_3', M_3'')—govern porous resistance, inertia, magnetization, and field-dependent viscosity effects. This structured scaling reflects the conventional hierarchy in magneto-convective stability analyses of porous nanofluids [3,9,31], where Ra and Rs serve as the primary bifurcation parameters, and other dimensionless groups modulate the critical thresholds.

4 Steady State Configuration

To establish the reference or base state, the system is assumed quiescent, with no macroscopic flow, i.e., $\boldsymbol{u}_b = \mathbf{0}$. Under this condition, the scalar variables p_b, T_b, ϕ_b, and C_b, together with the vector fields $\boldsymbol{H}_b$ and $\boldsymbol{M}_b$, are assumed to depend solely on the vertical coordinate z.

Inserting these steady state assumptions into the non-dimensional Eqs. (11)–(16) reduces the governing system to a set of coupled ordinary differential equations describing the equilibrium

distributions.

$$-\frac{dp_b}{dz}+\lambda_1 M_b\frac{dH_b}{dz}-Rn\phi_b+Ra\,T_b-Ra_N N_\phi\,T_b\phi_b-\frac{Rs}{Le_s}\,C_b+R_{sN}N_\phi\,\phi_b \times C_b+\rho_1\phi_b-\rho_2=0, \tag{18}$$

$$\frac{d^2\phi_b}{dz^2}+\frac{N_A}{Le}\frac{d^2T_b}{dz^2}-\frac{N'_A}{Le}\frac{d^2H_b}{dz^2}=0, \tag{19}$$

$$\frac{d^2T_b}{dz^2}+\left\{\frac{N_B}{Le}\frac{d\phi_b}{dz}+\frac{N_AN_B}{Le}\frac{dT_b}{dz}-\frac{N'_AN_B}{Le}\frac{dH_b}{dz}\right\}\frac{dT_b}{dz}+N_{TC}\frac{d^2C_b}{dz^2}=0, \tag{20}$$

$$\chi_2\frac{dM_b}{dz}+\frac{dH_b}{dz}=0, \tag{21}$$

$$M_b=\frac{1+\chi}{\chi_2}\left\{\frac{X}{1+X}H_b-\frac{M_T}{M_3}T_b+\frac{M'_1}{M'_3}\phi_b+\frac{M''_1}{M''_3}C_b+\frac{\chi_2-2\chi}{1+X}T_b\right\}, \tag{22}$$

$$\frac{1}{Le_S}\frac{d^2C_b}{dz^2}+N_{CT}\frac{d^2T_b}{dz^2}=0. \tag{23}$$

The steady state system is complemented by the boundary conditions specified in (17). Following the methodology outlined in earlier studies [21,22,32], closed–form expressions for the base-state fields can be obtained as

$$\boldsymbol{u}_b=0,\qquad p=p_b(z),\qquad T_b=\frac{T_h}{(T_h-T_c)}-z,\qquad \phi_b=\frac{\phi_0}{(\phi_0-\phi_1)}-z,$$
$$C_b=\frac{C_0}{(C_0-C_1)}-z,\qquad H_b=1-\frac{M_1}{M_3}z+\frac{M'_1}{M'_3}z+\frac{M''_1}{M''_3}z,$$
$$M_b=1+\frac{1}{\chi_2}\left(\frac{M_1}{M_3}\right)z-\frac{1}{\chi_2}\left(\frac{M'_1}{M'_3}\right)z-\frac{1}{\chi_2}\left(\frac{M''_1}{M''_3}\right)z. \tag{24}$$

To examine the stability of the base state, we introduce infinitesimal perturbations to all dependent variables:

$$\boldsymbol{u},\quad p,\quad T,\quad C,\quad \boldsymbol{M},\quad \phi,\quad \boldsymbol{H}.$$

Substituting the perturbed fields into the governing non–dimensional Eqs. (11)–(16) and linearizing about the steady state yields the following system of linearized equations.

$$\frac{1}{V_a}\frac{\partial\nabla^2 w}{\partial t}=-(1+\delta^*)\nabla^2 w-\left\{\frac{Ra\,M_3M'_1}{M'_3}+\frac{R_s\,M''_3M_1}{Le_s\,M_3}-N_g-Ra_N\left(1+N_\phi z\right)\right\}\nabla_1^2\theta$$
$$-\left\{\frac{Ra\,M_3M'_1}{M'_3}-\frac{R_s\,M''_3M'_1}{Le_s\,M'_3}-Ra_sM'_1+R_n+Ra_NN_\phi(1-z)-R_{sN}N_\phi(1-z)\right\}$$
$$\times\nabla_1^2\phi-\left\{RaM_3-Ra_sM'_3-\frac{R_s}{Le_s}M''_3\right\}\frac{\partial}{\partial z}\nabla_1^2\psi-\left\{\frac{R_s}{Le_s}\frac{M''_3M_1}{M_3}-\frac{R_s}{Le_s}\frac{M''_3M'_1}{M'_3}$$
$$-\frac{R_s}{Le_s}M''_1+R_{sN}\left(1+N_\phi z\right)\right\}\nabla_1^2C, \tag{25}$$

$$\frac{\partial \phi}{\partial t} = \frac{Pr}{DaV_a} w + \frac{1}{Le}\nabla^2\phi + \frac{N_A}{Le}\nabla^2\theta - \frac{N_A'}{Le}\frac{\partial}{\partial z}\nabla^2\psi, \tag{26}$$

$$A\frac{\partial \theta}{\partial t} = w + \nabla^2\theta - \left\{\frac{N_B}{Le} + \frac{2N_AN_B}{Le} - \frac{N_BN_A'M_1}{LeM_3} + \frac{N_BN_A'M_1'}{LeM_3'} + \frac{N_BN_A'M_1''}{LeM_3''}\right\}\frac{\partial \theta}{\partial z}$$
$$- \frac{N_B}{Le}\frac{\partial \phi}{\partial z} + \frac{N_BN_A'}{Le}\frac{\partial^2\psi}{\partial z^2} + N_{TC}\nabla^2 C, \tag{27}$$

$$\frac{\partial^2\psi}{\partial z^2} = \frac{M_1}{M_3}\frac{\partial \theta}{\partial z} - \frac{M_1'}{M_3'}\frac{\partial \phi}{\partial z} - \frac{M_1''}{M_3''}\frac{\partial C}{\partial z} - \frac{(1+\chi_2)}{(1+\chi)}\nabla_1^2\psi, \tag{28}$$

$$\frac{\partial C}{\partial t} = \frac{Pr}{DaV_a} w + \frac{1}{Le_S}\nabla^2 C + N_{CT}\nabla^2\theta. \tag{29}$$

Here $Ra_s = \dfrac{\rho_f g\alpha dK(\phi_0 - \phi_1)}{\mu\kappa}$, $Ng = M_1 Ra$ and $\delta^* = \mu_0\delta H_0(1+\chi_2)$ are the two non–dimensional numbers.

To enable eigenvalue analysis, the perturbations are decomposed into normal modes, represented by exponential functions of space and time.

$$[w, \phi, \theta, \psi, C] = [w(z), \phi(z), \theta(z), \psi(z), C(z)]\exp(\sigma t + i(k_x x + k_y y)). \tag{30}$$

Here k_x and k_y denote the horizontal wave numbers, with $k = \sqrt{k_x^2 + k_y^2}$ representing the resultant horizontal wavenumber. Substitution of the normal mode form into Eqs. (25)–(29) leads to the following reduced eigenvalue system.

$$\frac{\sigma}{V_a}(4D^2 - k^2)w(z) = -(1+\delta^*)(4D^2 - k^2)w(z) + \left\{Ra\frac{M_3M_1'}{M_3'} + \frac{Rs}{Les}\frac{M_3''M_1}{M_3} - Ra_N(1+N_\phi z)\right.$$
$$\left. -Ng\right\}k^2\theta(z) + \left\{Ra\frac{M_3M_1'}{M_3'} - \frac{Rs}{Les}\frac{M_3''M_1'}{M_3'} - Ra_sM_1' + Rn + Ra_NN_\phi(1-z) - Rs_NN_\phi\right.$$
$$\left.\times\ (1-z)\right\}k^2\phi(z) + \left\{RaM_3 - Ra_sM_3' - \frac{Rs}{Le_S}M_3''\right\}2Dk^2\psi(z) + \left\{\frac{Rs}{Le_S}\frac{M_3''M_1}{M_3} - \frac{Rs}{Le_S}\right.$$
$$\left.\times\frac{M_3''M_1'}{M_3'} - \frac{Rs}{Le_S}M_1'' + Rs_N(1+N_\phi z)\right\}k^2C(z), \tag{31}$$

$$\sigma\phi(z) = \frac{Pr}{D_aV_a}w(z) + \frac{1}{Le}(4D^2 - k^2)\phi(z) + \frac{N_A}{Le}(4D^2 - k^2)\theta(z) - \frac{2N_A'}{Le}$$
$$\times\ (4D^2 - k^2)D\psi(z), \tag{32}$$

$$A\sigma\theta(z) = w(z) + (4D^2 - k^2)\theta(z) - \left\{\frac{N_B}{Le} + \frac{2N_AN_B}{Le} - \frac{N_BN_A'M_1}{LeM_3} + \frac{N_BN_A'M_1'}{LeM_3'}\right.$$
$$\left. + \frac{N_BN_A'M_1''}{LeM_3''}\right\}2D\theta(z) - \frac{2N_B}{Le}D\phi(z) + \frac{4N_BN_A'}{Le}D^2\psi(z) + N_{TC}(4D^2 - k^2)C(z), \tag{33}$$

$$\left\{4D^2 - \frac{k^2(1+\chi_2)}{(1+\chi)}\right\}\psi(z) - \frac{2M_1}{M_3}D\theta(z) + \frac{2M_1'}{M_3'}D\phi(z) + \frac{2M_1''}{M_3''}DC(z) = 0, \tag{34}$$

$$\sigma C(z) = \frac{\mathrm{Pr}}{D_a V_a} w(z) + \frac{1}{Le_S}(4D^2 - k^2)C(z) + N_{CT}(4D^2 - k^2)\theta(z), \tag{35}$$

here $D = \dfrac{d}{dz}$ and $k = \sqrt{k_x^2 + k_y^2}$ is the wave number.

Closure of the linear system is achieved by imposing the boundary conditions:

$$\left.\begin{array}{llll} w = 0, & \theta = 0, & \phi = 0, & C = 0 \quad \text{at } z = \pm 1, \\ Dw = 0, & 2(1+\chi)D\psi - k\psi = 0 & & \text{at } z = -1, \\ D^2 w = 0, & 2(1+\chi)D\psi + k\psi = 0 & & \text{at } z = +1. \end{array}\right\} \tag{36}$$

The eigenvalue problem defined by Eqs. (31)–(35), together with the boundary conditions (36), is solved numerically using the Chebyshev pseudospectral method [33]. This technique offers spectral accuracy and rapid convergence for smooth solutions, making it particularly effective for stability analysis of convection problems. As a result, the computed eigenvalue spectrum provides a reliable determination of critical thresholds and transition behavior in the system. To match the Chebyshev pseudospectral-QZ domain, we map $[0, 1]$ to $[-1, 1]$ using the change $z \mapsto 2z - 1$.

Eigenvalue Behavior and Limiting Case Validation

To confirm the reliability of the linear stability results, eigenvalue sensitivity tests were carried out with respect to grid size, wavenumber spacing, and perturbation amplitude. The solution was considered converged when refining the collocation grid and reducing the wavenumber step led to less than a 0.5% variation in the critical Rayleigh number Ra_c. This ensured that the computed neutral curves and stability thresholds were independent of numerical resolution.

The model also reproduced well-known limiting behaviors (see Table 1). When either magnetic effects or field-dependent viscosity were suppressed ($M_1 = 0$ or $\delta = 0$), the system smoothly reduced to the standard Darcy-Buongiorno formulation, consistent with the expected FDV and nonmagnetic limits. In the fully nonmagnetic, double-diffusive case ($M_1 = M_3 = 0$), the critical Rayleigh number approached the classical benchmark for solutal-thermal convection in porous media [34]. In the purely thermal limit ($Rs = Rn = 0$), the neutral stability curve reduced to that of single-component Darcy convection with magnetic damping, in agreement with earlier studies [9,31].

Table 1: Validation of the present formulation via analytical and asymptotic limiting cases. All quantitative benchmarks shown are classical results; qualitative recoveries indicate that the present model reduces to the known limit without introducing new parameters or data

Limiting case	Reference condition (porous Darcy model)	Benchmark/Outcome
Pure thermal convection (Darcy-Bénard, RR)	$Rs = 0,\ Rn = 0,\ \delta = 0,\ M_1 = M_3 = 0$	$Ra_c = 4\pi^2 = 39.48$ (analytical)
Non-magnetic, double-diffusive porous limit (Buongiorno-type)	$M_1 = M_3 = 0,\ \delta = 0$	As $Les \to \infty$ and $Rs \to 0$, $Ra_c \to 4\pi^2$. For finite Rs, Rs stabilizes; Les destabilizes (qualitative recovery)

(Continued)

Table 1 (continued)

Limiting case	Reference condition (porous Darcy model)	Benchmark/Outcome
Magnetic + constant viscosity (porous, no FDV)	$\delta = 0,\ M_1, M_3 \neq 0$	Qualitative agreement: magnetic alignment raises Ra_c (no universal closed-form Ra_c in porous case)
FDV consistency check	$M_1, M_3 \neq 0,\ \delta > 0$	Increasing δ raises Ra_c; as $\delta \to 0$, model reduces to constant-viscosity limit (qualitative recovery)

5 Results and Discussion

To ensure parameter independence and consistent scaling, each non-dimensional group was varied individually while the remaining quantities were fixed at their baseline values. The thermal, solutal, and concentration Rayleigh numbers (Ra, Rs, Rn) govern the primary buoyancy forcing and therefore dominate the onset of convection. The Langevin parameter (α_L), field-dependent viscosity coefficient (δ), and Darcy number (Da) introduce secondary stabilizing influences through magnetic alignment, magnetoviscous damping, and porous resistance, respectively. In contrast, the solutal Lewis number (Les) promotes destabilization by enhancing the imbalance between thermal and solutal diffusion. Across all Figs. 2–7, these behaviors establish a consistent qualitative hierarchy of influence: the strongest control arises from the buoyancy parameters (Ra, Rs, R_n), followed by magnetic and viscous modifiers (α_L, δ, Da), while diffusive transport (Les) exerts a comparatively weaker effect. This ordering reflects the progressive transition from thermally dominated to diffusion-controlled behavior, in agreement with established porous–magnetoconvective analyses [3,9,31].

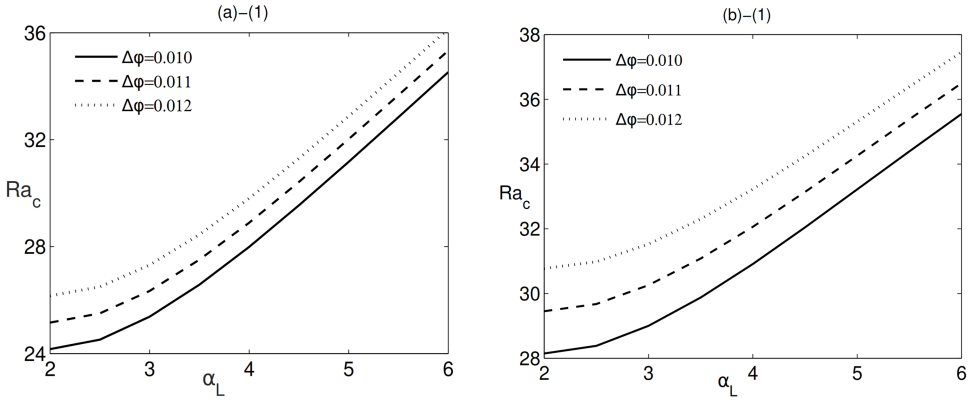

Figure 2: Variation of the critical Rayleigh number Ra_c with the Langevin parameter α_L for (a)-(1) W_b–MNF and (b)-(1) E_b–MNF under rigid-free boundary conditions. The solid, dashed, and dotted curves correspond to magnetic nanoparticle concentration differences $\Delta\phi = 0.010$, 0.011, and 0.012, respectively. Both axes are dimensionless

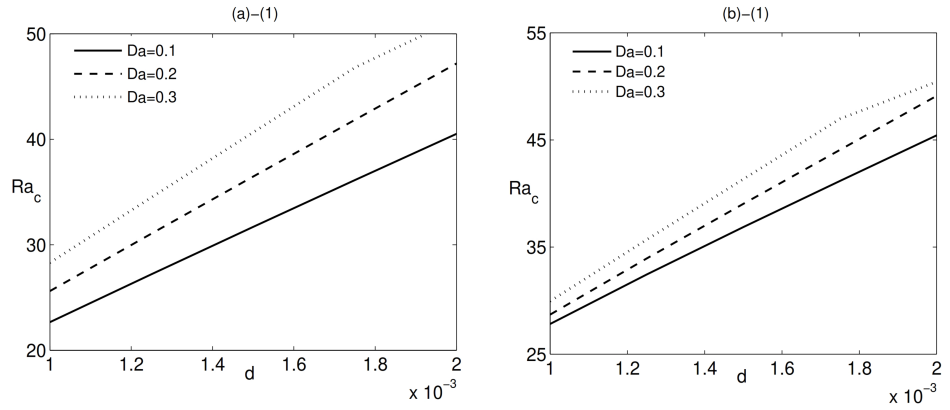

Figure 3: Variation of the critical Rayleigh number Ra_c with the layer thickness d for (a)-(1) W_b–MNF and (b)-(1) E_b–MNF under rigid-free boundary conditions. The solid, dashed, and dotted curves correspond to Darcy number values $Da = 0.1$, 0.2, and 0.3, respectively. Both axes are dimensionless

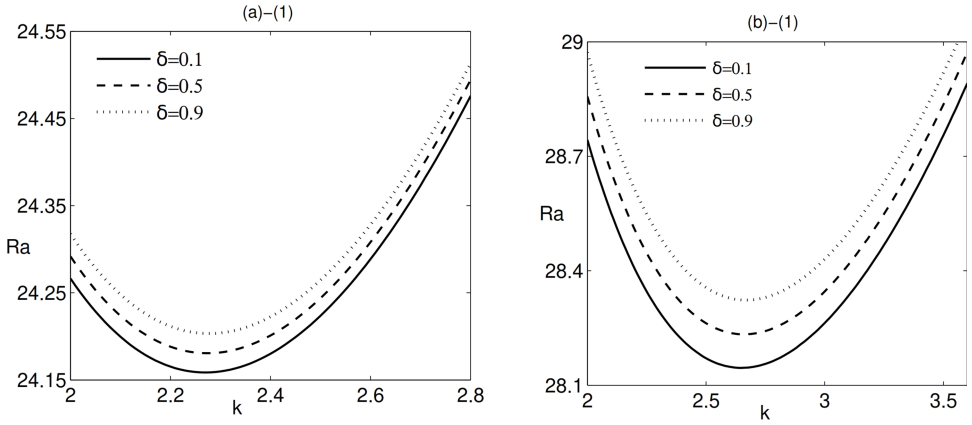

Figure 4: Neutral stability curves showing the dependence of the Rayleigh number Ra on the wavenumber k for (a) W_b–MNF and (b) E_b–MNF under rigid-free boundary conditions. The solid, dashed, and dotted lines correspond to $\delta = 0.1$, 0.5, and 0.9, respectively. The minimum of each curve identifies the critical state (Ra_c, k_c) marking the onset of stationary convection. Both axes are dimensionless

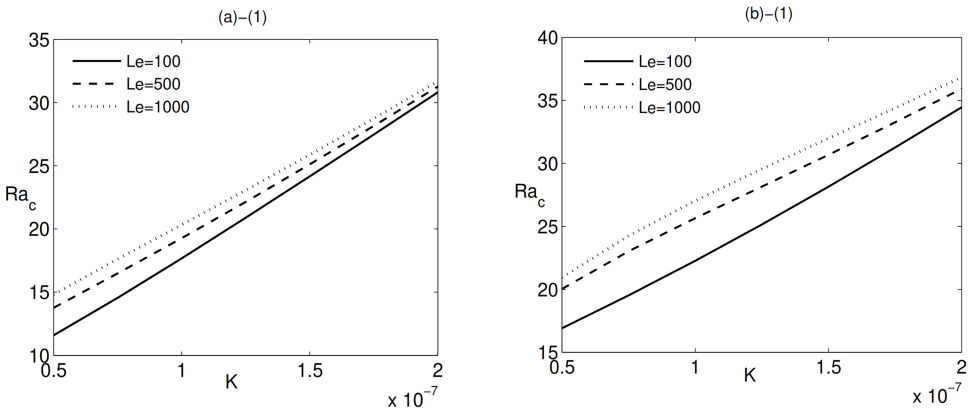

Figure 5: Variation of the critical Rayleigh number Ra_c with the permeability parameter K for (a)-(1) W_b–MNF and (b)-(1) E_b–MNF under rigid-free boundary conditions. The solid, dashed, and dotted curves correspond to Lewis number values $Le = 100$, 500, and 1000, respectively. Both axes are dimensionless

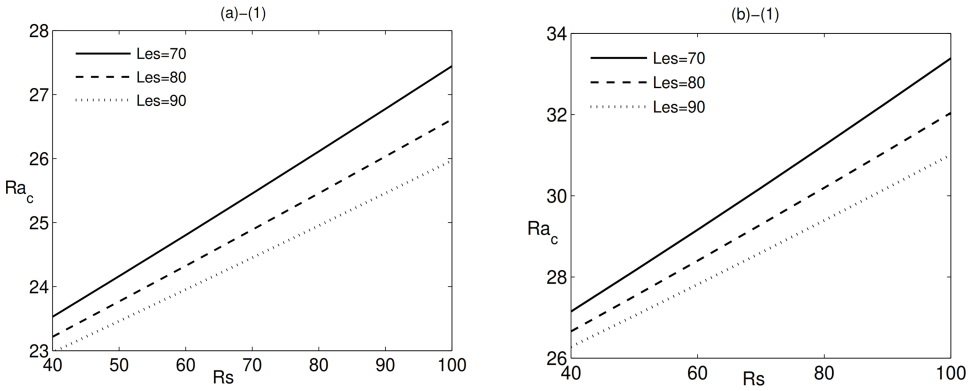

Figure 6: Variation of the critical Rayleigh number Ra_c with the solutal Rayleigh number Rs for (a)-(1) W_b–MNF and (b)-(1) E_b–MNF under rigid-free boundary conditions. The solid, dashed, and dotted curves correspond to modified Lewis number values $Les = 70$, 80, and 90, respectively. Both axes are dimensionless

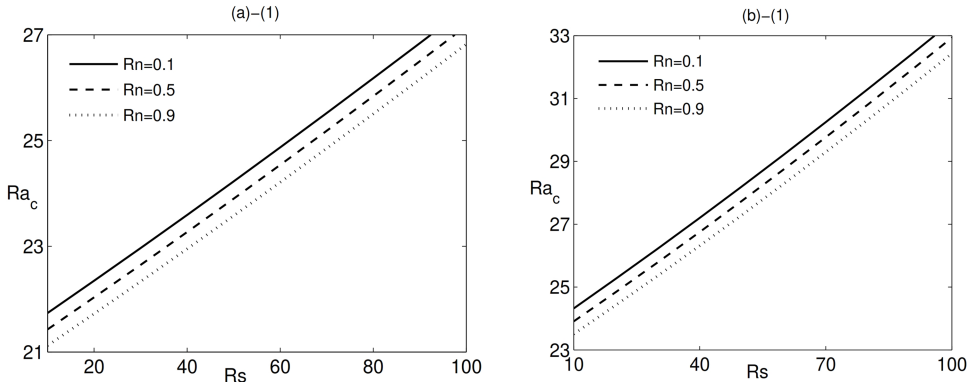

Figure 7: Variation of the critical Rayleigh number Ra_c with the solutal Rayleigh number Rs for (a)-(1) W_b–MNF and (b)-(1) E_b–MNF under rigid-free boundary conditions. The solid, dashed, and dotted curves correspond to values of concentration Rayleigh number $Rn = 0.1$, 0.5, and 0.9, respectively. Both axes are dimensionless

For the present analysis, numerical computations are carried out for a 1 mm thick horizontal layer of W_b-MNF and E_b-MNF. The thermophysical properties of the base fluids and nanoparticles are adopted from standard references [8,35]. The model assumes spherical nickel (Ni) nanoparticles of diameter 10 nm uniformly dispersed in the carrier fluid, which saturates a porous medium of low permeability. The porous matrix is characterized by a porosity $\epsilon = 0.35$ and a permeability $K = 1.5 \times 10^{-7}$ m^2.

5.1 Quantitative Interpretation and Scaling Analysis

Langevin parameter α_L and concentration difference $\Delta\phi$ (Fig. 2). The critical Rayleigh number (Ra_c) increases monotonically with α_L for both W_b– and E_b–MNF, indicating enhanced stability. Physically, a higher α_L strengthens magnetic dipole alignment with the applied field, increasing the magnetization contribution in the momentum balance and suppressing velocity perturbations. The stabilizing influence is amplified at larger $\Delta\phi$, as higher nanoparticle loading elevates the magnetic body force; this appears as a uniform upward shift of the $Ra_c(\alpha_L)$ curves for increasing $\Delta\phi$. The trend is slightly stronger for E_b–MNF, consistent with its higher carrier viscosity and attendant viscous damping.

Nanofluid layer thickness (d) and Darcy number (Da) (Fig. 3). Fig. 3 illustrates the dependence of the critical Rayleigh number (Ra_c) on the nanofluid layer thickness (d) for different values of the Darcy number (Da). For all examined cases, Ra_c increases monotonically with d, indicating a stabilizing effect. As the fluid layer becomes thicker, a stronger thermal gradient is required to initiate convection. This trend arises from the enhanced viscous and magnetic resistance encountered by perturbations traversing a larger vertical extent, particularly within a porous matrix exhibiting magnetoviscous coupling.

For a given d, higher values of Da also lead to larger Ra_c, further reinforcing system stability. Although a larger Darcy number generally signifies increased permeability and reduced mechanical drag, the present results reveal that field-dependent viscosity and magnetic alignment exert dominant stabilizing influences, effectively counteracting permeability-driven flow facilitation.

Between the two base fluids, E_b-MNF consistently exhibits higher Ra_c than W_b-MNF across all d and Da, owing to its higher viscosity and lower nanoparticle diffusivity. These attributes enhance momentum damping and suppress the onset of convection. Overall, the combined effects of d and Da highlight the intricate balance between geometric confinement and magnetic-porous resistance, underscoring their pivotal role in governing convective stability in magnetized nanofluid-saturated porous systems.

Field-dependent viscosity coefficient δ (Fig. 4). The neutral stability curves shift upward as δ increases, and the minimum remains at finite k, confirming a stationary onset. Over the examined range ($\delta = 0.1$–0.9), Ra_c increases by approximately 0.2%–2%, indicating mild but consistent stabilization. This behavior reflects the additional viscous resistance introduced by the FDV term through the factor $\delta^* = \mu_0\, \delta\, H_0(1 + \chi_2)$, which augments dissipation in the momentum balance.

Permeability parameter *(K)* and critical Rayleigh number (R_{ac}) (Fig. 5). Fig. 5 illustrates the variation of the critical Rayleigh number R_{ac} with the permeability parameter K for W_b–MNF and E_b–MNF under rigid–free boundary conditions. For both nanofluids, R_{ac} increases monotonically with K, indicating that higher permeability raises the threshold for the onset of convection. The curves corresponding to $Le = 100$, 500, 1000 follow a consistent ordering, with larger Le producing larger R_{ac} due to enhanced solutal diffusion effects. Across all K, the E_b–MNF exhibits higher R_{ac} than the W_b–MNF, reflecting its greater effective viscosity and lower thermal diffusivity.

Solutal Lewis number (*Les*) and solutal Rayleigh number (*Rs*) (Fig. 6). The interplay between Les and Rs governs solutal transport and compositional stability in the porous MNF system. For a fixed Les, the critical Rayleigh number Ra_c increases monotonically with Rs, reflecting the stabilizing effect of solutal stratification. A stronger solutal gradient resists vertical motion of fluid parcels and increases the energy barrier for convection.

Conversely, for a given Rs, larger Les values ($70 \rightarrow 90$) reduce Ra_c, indicating that weaker solutal diffusion enhances residual concentration gradients and promotes earlier instability. The combined trends demonstrate that Rs primarily sets the strength of solutal resistance, while Les regulates its diffusion-driven relaxation. The effect is slightly more pronounced in E_b-MNF, where lower solutal diffusivity and higher viscosity amplify the compositional damping. These coupled behaviors are consistent with classical double-diffusive convection in porous nanofluids, confirming that Rs stabilizes and Les destabilizes the onset of convection.

Concentration Rayleigh number *Rn* (Fig. 7). Rn consistently decreases Ra_c, signifying destabilization. Stronger nanoparticle concentration gradients amplify buoyancy and promote the onset of convection. The reduction is more evident for W_b-MNF, consistent with higher particle mobility and thermal conductivity.

Influence of Boundary Conditions and Base Fluid

This section assesses the combined influence of mechanical boundary conditions and base-fluid properties on the stability threshold, as detailed in Table 2.

Table 2: Critical wavenumber (k_c) and critical Rayleigh number (Ra_c) for MNFs in a porous layer under different boundary conditions (RR, RF, FF) and fluid types (W_b, E_b), for varying *Les* and δ

		RR		*RF*				*FF*					
		W_b		E_b		W_b		E_b		W_b		E_b	
Les	δ	k_c	Ra_c	k_c	Ra_c	k_c	Ra_c	k_c	Ra_c	k_c	Ra_c	k_c	Ra_c
70	0.01	2.3	24.16	2.6	28.13	2.0	23.85	2.1	27.83	1.6	15.16	1.6	16.96
	0.21	2.3	24.17	2.7	28.17	2.0	23.95	2.1	27.85	1.6	15.22	1.6	17.04
	0.41	2.3	24.18	2.7	28.22	2.0	24.05	2.1	27.87	1.6	15.28	1.6	17.13
	0.61	2.3	24.19	2.7	28.26	2.0	24.15	2.1	27.90	1.6	15.34	1.6	17.21
	0.81	2.3	24.20	2.7	28.30	2.0	24.25	2.1	27.92	1.6	15.40	1.6	17.29
	0.93	2.3	24.21	2.7	28.33	2.0	24.31	2.1	27.94	1.6	15.43	1.6	17.34
	0.97	2.3	24.21	2.7	28.34	2.0	24.33	2.1	27.94	1.6	15.44	1.6	17.35
80	0.01	2.3	23.76	2.7	27.50	2.0	23.57	2.1	27.19	1.6	14.91	1.6	16.63
	0.21	2.3	23.77	2.7	27.55	2.0	23.67	2.1	27.21	1.6	14.97	1.6	16.71
	0.41	2.3	23.78	2.7	27.59	2.0	23.77	2.1	27.23	1.6	15.02	1.6	16.79
	0.61	2.3	23.79	2.7	27.64	2.0	23.88	2.1	27.26	1.6	15.08	1.6	16.87
	0.81	2.3	23.80	2.7	27.68	1.9	23.98	2.1	27.28	1.6	15.14	1.6	16.95
	0.93	2.3	23.81	2.7	27.71	1.9	24.04	2.1	27.30	1.6	15.18	1.6	17.00
	0.97	2.3	23.81	2.7	27.72	1.9	24.05	2.1	27.31	1.6	15.19	1.6	17.02
90	0.01	2.3	23.45	2.7	27.02	2.0	23.36	2.1	26.69	1.6	14.72	1.6	16.38
	0.21	2.3	23.46	2.7	27.07	2.0	23.46	2.1	26.72	1.6	14.78	1.6	16.47
	0.41	2.3	23.48	2.7	27.11	1.9	23.56	2.1	26.75	1.6	14.84	1.6	16.55
	0.61	2.3	23.49	2.7	27.16	1.9	23.66	2.1	26.77	1.6	14.90	1.6	16.63
	0.81	2.3	23.50	2.7	27.21	1.9	23.76	2.1	26.80	1.6	14.96	1.6	16.71
	0.93	2.3	23.51	2.7	27.24	1.9	23.82	2.1	26.82	1.6	14.99	1.6	16.76
	0.97	2.3	23.51	2.7	27.24	1.9	23.84	2.1	26.82	1.6	15.00	1.6	16.77

Effect of Boundary Conditions: A strong, predictable hierarchy in stability is observed across the mechanical boundary configurations. The Rigid–Rigid (RR) case consistently yields the highest Ra_c values, as the no-slip boundary condition imposes maximal mechanical resistance to flow. Conversely, the Free–Free (FF) condition yields the lowest Ra_c (e.g., $Ra_c = 15.39$ for W_b–MNF), reflecting minimal shear-stress resistance and the earliest onset of convection. The transition from RR to FF results in an approximately 35.4% reduction in Ra_c for the water-based system, confirming the critical role of mechanical constraints as a dominant stabilizing factor. The corresponding wavenumber (k_c) is highest for RR, indicating that constrained boundaries enforce a finer convective-cell structure at instability onset.

Comparison of Base Fluids: The E_b–MNF consistently exhibits enhanced resistance to convection compared with the W_b–MNFs. The E_b–MNF system displays Ra_c values that are approximately 19.9% higher across all boundary configurations. This stabilizing effect arises from the inherently higher

viscosity and lower thermal diffusivity of the ester base, which increase viscous damping and require a larger thermal driving force (higher Ra_c) to initiate buoyant motion.

Asymptotic limits. In the limit $\delta \to 0$, the formulation recovers the classical Buongiorno-type double-diffusive model without field-dependent viscosity. Likewise, as $Le_s \to \infty$, solutal diffusion becomes negligible and Ra_c asymptotically approaches the thermal-only instability threshold, demonstrating the model's consistency with established physical limits.

5.2 Comparative Analysis with Previous Studies

FDV-induced stabilization is consistent with previous porous- and ferroconvection analyses that incorporated magnetoviscous effects [4]. Similarly, the destabilization observed for larger *Les* and *Rn*, and the modest stabilization with *Rs*, correspond well with double-diffusive nanofluid studies highlighting the competition between solutal diffusion and compositional buoyancy [5,36]. The present results extend these earlier findings by demonstrating, within a unified framework, the coupled influence of FDV, magnetic alignment (through α_L and $\Delta\phi$), and porous-medium resistance on convective stability.

5.3 Computational Consistency Note

Spectral discretization. The eigenvalue problem was solved using a Chebyshev pseudospectral–QZ method, which is widely recognized for its high accuracy in stability problems involving smooth eigenfunctions. The choice of this scheme ensures efficient resolution of sharp gradients in the eigenstructure without excessive computational overhead.

Numerical confidence. In this study, $N = 60$ Chebyshev collocation points were used, which falls within the standard range for achieving spectral accuracy in similar linear stability problems. This choice balances numerical resolution with computational efficiency. Preliminary trials with higher resolution did not significantly change the computed critical Rayleigh number, supporting the adequacy of this resolution.

5.4 Post–Analysis Validation and Benchmark Comparison

To reinforce the reliability of the obtained eigenvalue spectra and parametric trends, an additional analytical validation is performed by comparing the computed thresholds with classical benchmarks. In the limiting case $\delta = 0$ and $Rs = 0$, the model reduces to classical thermal convection in a porous layer. For rigid–rigid (RR) boundaries, this limit yields the well-known benchmark threshold $Ra_{c,\mathrm{th}} = 4\pi^2 \approx 39.48$, consistent with the Darcy-Bénard onset under constant viscosity and purely thermal forcing [34]. This serves as a rigorous analytical check on the model framework.

By contrast, the full-physics model incorporating magnetization (α_L), particle concentration difference ($\Delta\phi$), field-dependent viscosity (through δ), and double-diffusive effects (*Les, Rs, Rn*) predicts a significantly lower threshold. For example, $Ra_c \approx 23.78$ is obtained for ($\delta = 0.41$, $Les = 80$, $Rs = 60$) under RR boundaries (Table 2), confirming that the combined magnetic and solutal effects destabilize the system, causing convection to set in at a smaller temperature gradient compared to the purely thermal Darcy case.

Within this overall destabilized regime, however, individual parameters exert contrasting influences: increasing δ, α_L, or $\Delta\phi$ raises Ra_c (stabilizing), whereas higher *Les* enhances double—diffusive coupling and thus lowers Ra_c (destabilizing), while *Rs* acts oppositely—its increase suppresses convection and stabilizes the system. The corresponding neutral stability curves, shown in Figs. 4 and 6,

capture these opposing trends. This consistency between asymptotic limits, tabulated thresholds, and graphical results validates the correctness of the numerical implementation.

5.5 Summary

The Langevin parameter (α_L), field-dependent viscosity coefficient (δ), Darcy number (Da), and solutal Rayleigh number (Rs) act as stabilizing influences by strengthening magnetic alignment, enhancing viscous damping, and reinforcing solutal stratification. In contrast, the solutal Lewis number (Les) and concentration Rayleigh number (Rn) promote earlier onset through diffusion imbalance and concentration-driven buoyancy. An increase in nanoparticle concentration difference ($\Delta\phi$) magnifies both magnetic and FDV effects, further shifting the stability threshold.

The critical wavenumber k_c remains nearly invariant across boundary conditions and δ, indicating that these parameters primarily raise the energy barrier for instability rather than altering the dominant convective scale. The limiting cases $\delta \to 0$ and $Les \to \infty$ recover the classical Darcy–Bénard and Buongiorno-type behaviors, confirming the internal consistency of the formulation. Grid-refinement tests and spectral-convergence assessments verify numerical independence, while the agreement between asymptotic limits, tabulated thresholds, and neutral-curve trends supports the reliability of the computed results.

Overall, the findings delineate a physically consistent stability framework for magnetized nanofluid-saturated porous systems. They highlight how the coupled action of magnetic alignment, field-dependent viscosity, and double-diffusive transport governs the transition from conductive equilibrium to convective motion, providing a validated reference for future experimental and numerical studies on magnetic nanofluid convection.

6 Conclusions

This study presents a comprehensive linear stability analysis of double–diffusive convection in magnetic nanofluids (MNFs) saturated within a horizontal porous medium, explicitly accounting for field–dependent viscosity (FDV), magnetization (via the Langevin parameter α_L), and solutal transport effects. The combined action of magnetophoretic, thermophoretic, and solutal mechanisms fundamentally destabilizes the system, yielding a critical thermal Rayleigh number $Ra_c \approx 23.78$ for representative base–case parameters ($\delta = 0.41$, $Les = 80$, $Rs = 60$) under rigid–rigid boundaries. This threshold is substantially lower than the classical Darcy–Bénard limit $Ra_{c,\mathrm{th}} = 4\pi^2 \approx 39.48$, confirming that the inclusion of coupled magnetic and solutal physics induces convection at smaller temperature differences.

Within this overall destabilized regime, individual parameters exhibit contrasting influences. Increases in the FDV coefficient (δ), Langevin parameter (α_L), and nanoparticle concentration difference ($\Delta\phi$) raise Ra_c, indicating their stabilizing roles through enhanced viscous and magnetic damping. Conversely, a higher solutal Lewis number (Les) reduces Ra_c by amplifying double–diffusive coupling, while the solutal Rayleigh number (Rs) exerts a stabilizing influence by reinforcing solutal stratification. The concentration Rayleigh number (Rn) remains a dominant destabilizing factor, with stronger compositional buoyancy promoting earlier onset of convection.

Boundary conditions and base–fluid properties further modulate stability characteristics. Rigid–rigid configurations yield the highest thresholds due to enhanced mechanical resistance, while free–free conditions trigger convection earliest. Among base fluids, ester–based MNFs consistently display 15%–20% higher Ra_c values than water–based MNFs, reflecting their greater viscosity and reduced

thermal diffusivity. These systematic trends across analytical limits, tabulated thresholds, and neutral–curve behaviors confirm the reliability and internal consistency of the developed model.

Overall, the results delineate a validated physical framework for controlling convective onset in magnetized nanofluid–saturated porous systems. The interplay of FDV, magnetic alignment, and solutal diffusion governs the transition from conduction to convection, offering predictive guidance for the design of porous heat exchangers, magnetothermal filters, and energy–efficient thermal management systems.

Limitations and Future Directions

This work is based on an idealized model that assumes a homogeneous, isotropic porous matrix governed by Darcy flow. The analysis excludes pore-scale heterogeneity, anisotropic permeability, and non-Darcian effects that may become significant at high velocities. It also neglects thermal non-equilibrium between the fluid and solid phases and potential multiphase dynamics. Future investigations should incorporate more realistic porous structures, explore the influence of Brinkman and Forchheimer corrections, and assess nonlinear and time-dependent instabilities. Experimental validation and pore-scale simulations would further enhance the model's applicability to real-world thermal management systems involving magnetic nanofluids.

Acknowledgement: The authors gratefully acknowledge the support provided by their respective institutions.

Funding Statement: This work was conducted without any specific grant from funding agencies in the public, commercial, or not-for-profit sectors.

Author Contributions: The study was conceptualized and executed by the first author. Monika Arora contributed to the development of the methodology and performed the analysis. The manuscript was drafted by Monika Arora, and Mahesh Kumar Sharma participated in the review and editing process. All authors reviewed the results and approved the final version of the manuscript.

Availability of Data and Materials: This study is theoretical and does not involve any data or materials.

Ethics Approval: Not applicable.

Conflicts of Interest: The authors declare no conflicts of interest to report regarding the present study.

References

1. Humnekar N, Srinivasacharya D. Influence of variable viscosity and double diffusion on the convective stability of a nanofluid flow in an inclined porous channel. Appl Math Mech (English Edition). 2024;45(3):563–80. doi:10.1007/s10483-024-3096-6.
2. Chuhan IS, Li J, Ahmed MS, Samuilik I, Aslam MA, Manan MA. Numerical investigation of double-diffusive convection in an irregular porous cavity subjected to an inclined magnetic field using the finite element method. Mathematics. 2024;12(6):808. doi:10.3390/math12060808.
3. Nield DA, Kuznetsov AV. The onset of double-diffusive convection in a nanofluid layer. Int J Heat Fluid Flow. 2011;32(4):771–6. doi:10.1016/j.ijheatfluidflow.2011.03.010.
4. Sharma MK, Singh R. Linear stability analysis of double-diffusive convection in magnetic nanofluids in porous media. J Porous Media. 2014;17(10):883–900. doi:10.1615/jpormedia.v17.i10.40.

5. Mahajan A, Sharma MK. Double-diffusive convection in a magnetic nanofluid layer with cross-diffusion effects. J Eng Math. 2019;115(1):67–87. doi:10.1007/s10665-019-09992-8.
6. Sunil, Sharma P, Mahajan A. A nonlinear stability analysis of a double-diffusive magnetized ferrofluid. Appl Math Comput. 2011;218(6):2785–99. doi:10.1016/j.amc.2011.08.021.
7. Choi SUS. Enhancing thermal conductivity of fluids with nanoparticles. Proc ASME Int Mech Eng Congr Expo. 1995;66:99–105.
8. Rosensweig RE. Ferrohydrodynamics. New York, NY, USA: Dover Publications; 1985.
9. Finlayson BA. Convective instability of ferromagnetic fluids. J Fluid Mech. 1970;40(4):753–67. doi:10.1017/s0022112070000423.
10. Vaidyanathan G, Sekar R, Vasanthakumari R, Ramanathan A. The effect of magnetic field dependent viscosity on ferroconvection in a rotating sparsely distributed porous medium. J Magn Magn Mater. 2002;250(2):65–76. doi:10.1016/s0304-8853(02)00355-4.
11. Sunil, Divya, Sharma RC. The effect of magnetic field dependent viscosity on thermosolutal convection in a ferromagnetic fluid saturating a porous medium. Transp Porous Media. 2005;60(3):251–74. doi:10.1007/s11242-004-5739-y.
12. Arora M, Sharma MK, Danesh M. Effect of rotation and magnetic-field-dependent viscosity on the onset of convection in magnetic nanofluids. AIP Conf Proc. 2023;2652(1):030036. doi:10.1063/5.0196199.
13. Blums E, Cebers A, Maiorov MM. Magnetic fluids. Berlin, Germany: De Gruyter; 2008.
14. Mahajan A, Sharma MK. Thermomagnetic convection in a layer of magnetic nanofluid saturating porous medium with magnetic-field-dependent viscosity. Int J Nanopart. 2019;11(3):181. doi:10.1504/ijnp.2019.102586.
15. Ganesh NV, Al-Mdallal QM, Abbasbandy S, Sarris IE. Influence of magnetic-field-dependent viscosity on Casson-based nanofluid boundary layers: lie group and spectral quasi-linearisation analysis. Heliyon. 2024;10(7):e28994. doi:10.1016/j.heliyon.2024.e28994.
16. Shoaib M, Raja MAZ, Sabir MT, Islam S, Shah Z, Kumam P, et al. Numerical investigation for rotating flow of MHD hybrid nanofluid with thermal radiation over a stretching sheet. Sci Rep. 2020;10(1):18533. doi:10.1038/s41598-020-75254-8.
17. Dhananjay Y, Bhargava R, Agrawal G. Thermal instability in a nanofluid layer with a vertical magnetic field. J Eng Math. 2013;80(1):147–64. doi:10.1007/s10665-012-9598-1.
18. Saran HL, RamReddy C. Analysis of aligned magnetic field, flow separation, and stability in a porous medium saturated by hybrid nanofluids. J Therm Anal Calorim. 2023;148(9):3765–81. doi:10.1007/s10973-023-11946-3.
19. Syam MM. Thermal and fluid behavior of nanofluids over a rotating disk: influence of Darcy-Forchheimer and slip conditions. Int J Thermofluids. 2025;28(2):101316. doi:10.1016/j.ijft.2025.101316.
20. Haq EU, Khan SU, Abbas T, Smida K, Hassan QM U, Ahmad B, et al. Numerical aspects of thermo-migrated radiative nanofluid flow towards a moving wedge with combined magnetic force and porous medium. Sci Rep. 2022;12(1):10120. doi:10.1038/s41598-022-14259-x.
21. Buongiorno J. Convective transport in nanofluids. J Heat Transf. 2006;128(3):240–50. doi:10.1115/1.2150834.
22. Nield DA, Kuznetsov AV. The onset of convection in a horizontal nanofluid layer of finite depth. Euro J Mech B/Fluids. 2010;29(3):217–23. doi:10.1016/j.euromechflu.2010.02.003.
23. Umavathi JC, Sheremet MA, Ojjela O, Reddy GJ. The onset of double-diffusive convection in a nanofluid-saturated porous layer: cross-diffusion effects. Euro J Mech B/Fluids. 2017;65(1):70–87. doi:10.1016/j.euromechflu.2017.01.017.
24. Yadav D, Lee D, Cho HH, Lee J. The onset of double-diffusive nanofluid convection in a rotating porous medium layer with thermal conductivity and viscosity variation: a revised model. J Porous Media. 2016;19(1):31–46. doi:10.1615/jpormedia.v19.i1.30.

25. Rajenderan E, Prasad VR. Numerical study of magneto-convective Ag-graphene oxide hybrid nanofluid in a square enclosure with hot and cold slits and internal heat generation/absorption. Sci Rep. 2024;14(1):24868. doi:10.1038/s41598-024-76233-z.
26. Diwania S, Kumar M, Kumar R, Kumar A, Gupta V, Khetrapal P. Machine learning-based thermo-electrical performance improvement of nanofluid-cooled photovoltaic-thermal system. Energy Environ. 2024;35(4):1793–817. doi:10.1177/0958305x221146947.
27. Asifa, Anwar T, Kumam P, Almutairi KS, Watthayu W. Thermophysical dynamics of mineral-oil-based hybrid nanofluids under multiple flow conditions and radiation effects: individual, synergistic, and shape impacts analysis. J Radiat Res Appl Sci. 2025;18(4):101748. doi:10.1016/j.jrras.2025.101748.
28. Arif K, Saeed ST, Anwar T, Abbas S, Aslam MN. Numerical investigation for optimizing thermal performance of Al_2O_3-TiO_2/water hybrid nanofluid: an artificial neural network approach based on the Levenberg-Marquardt algorithm. Int J Thermofluids. 2025;29(4):101360. doi:10.1016/j.ijft.2025.101360.
29. Syam MM, Alabdul Razzak M, Ammar HR, Aldeleh SS. Nonlinear dynamics of laminar flow in porous channels: effects of wall dilation and inertial-viscous interplay. Int J Thermofluids. 2025;27(3):101259. doi:10.1016/j.ijft.2025.101259.
30. Souad M, Mebarek-Oudina F, Magherbi M, Mchirgui A. Entropy generation and heat transport of Cu-water nanoliquid in a porous lid-driven cavity under a magnetic field. Int J Numer Methods Heat Fluid Flow. 2022;32(6):2047–69. doi:10.1108/hff-04-2021-0288.
31. Dogonchi AS, Seyyedi SM, Hashemi-Tilehnoee M, Chamkha AJ, Ganji DD. Investigation of natural convection of magnetic nanofluid in an enclosure with a porous medium considering Brownian motion. Case Stud Therm Eng. 2019;14(4):100502. doi:10.1016/j.csite.2019.100502.
32. Arora M, Singh R, Panda MK. Effects of magnetic-field-dependent viscosity at onset of convection in magnetic nanofluids. J Eng Math. 2016;101(1):201–17. doi:10.1007/s10665-016-9855-9.
33. Canuto C, Hussaini MY, Quarteroni A, Zang T. Spectral methods in fluid dynamics. New York, NY, USA: Springer; 1998.
34. Nield DA, Bejan A. Convection in porous media. 5th ed. New York, NY, USA: Springer; 2017.
35. Kaloni PN, Lou JX. Convective instability of ferrofluids with internal heating. Phys Rev E. 2004;70:026313.
36. Malashetty MS, Biradar RS. The onset of double-diffusive convection in a Maxwell fluid with cross-diffusion effects. Int J Heat Mass Transf. 2011;54(6):527–36. doi:10.1063/1.3601482.